Segmentation of Overlapping Elliptical Objects in Silhouette Images

Sahar Zafari, Tuomas Eerola, Jouni Sampo, Heikki Kälviäinen, and Heikki Haario

Abstract—**Segmentation of partially overlapping objects with a known shape is needed in an increasing amount of various machine vision applications. This paper presents a method for segmentation of clustered partially overlapping objects with a shape that can be approximated using an ellipse. The method utilizes silhouette images, which means that it requires only that the foreground (objects) and background can be distinguished from each other. The method starts with seedpoint extraction using bounded erosion and fast radial symmetry transform. Extracted seedpoints are then utilized to associate edge points to objects in order to create contour evidence. Finally, contours of the objects are estimated by fitting ellipses to the contour evidence. The experiments on one synthetic and two different real data sets showed that the proposed method outperforms two current state-of-art approaches in overlapping objects segmentation.**

Index Terms—**Segmentation, overlapping objects, convex objects, image processing, machine vision.**

I. INTRODUCTION

SEGMENTATION of overlapping objects aims to address the issue of representation of multiple objects with partial views. Overlapping or occluded objects occur in various applications, such as morphology analysis of molecular or cellular objects in biomedical and industrial imagery where quantitative analysis of individual objects by their size and shape is desired [1]–[3]. In many such applications, the objects can often be assumed to contain approximately elliptical shape. For example, the most commonly measured properties of nanoparticles are their length and width, which can correspond to the major and minor axis of an ellipse fitted over the particle contour [4].

Even with rather strong shape priors, segmentation of overlapping objects remains a challenging task.
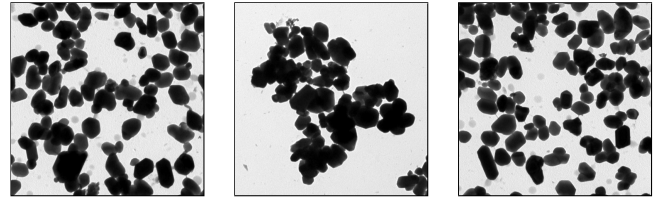
Fig. 1. Overlapping crystal particles.

Deficient information from the objects with occluded or overlapping parts introduces considerable complexity into the segmentation process. For example, in the context of contour estimation, the contours of objects intersecting with each other do not usually contain enough visible geometrical evidence, which can make contour estimation problematic and challenging. Frequently, the segmentation method has to rely purely on edges between the background and foreground, which makes the processed image essentially a silhouette image (see Fig. 1). Furthermore, the task involves simultaneous segmentation of multiple objects. A large number of objects in the image causes a large number of variations in pose, size and shape of the objects, and leads to a more complex segmentation problem.

In this paper, a method is proposed for the segmentation of partially overlapping objects whose approximate shape are known. The objects to be segmented are assumed to be clearly distinguishable from the background of the image and their contours form approximately elliptical shapes. The proposed method is an edge based segmentation approach that follows three sequential steps: namely, seedpoint extraction, contour evidence extraction, and contour estimation. Seedpoint extraction is performed by a compound model consisting of morphological erosion [5] and the Fast Radial Symmetry (FRS) transform [6]. The contour evidence extraction links the object seedpoints and the edge map obtained from the image. To perform this connection, a metric similar to [1] using the distance between seed and edge points combined with the cosine distance between the gradient and seed-to-edge vectors is sought. Once the contour evidence for each detected seedpoint is obtained, contour estimation is performed using numerically stable direct ellipse fitting.

The work makes two contributions to study of machine vision and object segmentation. The first contribution of this work is the combined method of Bounded Erosion-Fast Radial Symmetry (BE-FRS) for seedpoint extraction from a group of highly overlapping objects in silhouette images. Based on observed general convexity and radial symmetry of the
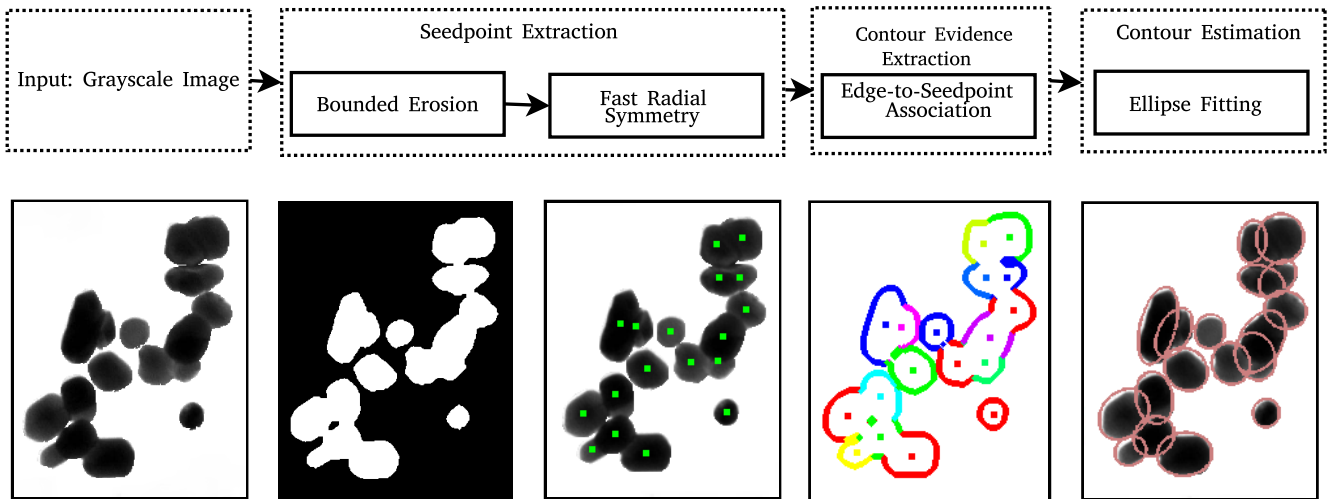
Fig. 2. Proposed method.

overlapping objects, the proposed BE-FRS method incorporates a predefined number of morphological erosion operations to eliminate the touching points and increase the convexity of objects and Fast Radial Transform [6] to extract the intersection of the lines of symmetry as individual centroids. The second contribution is integration of the proposed BE-FRS method into the segmentation of overlapping convex objects, enabling improvements compared to existing methods with higher detection rate and segmentation accuracy.

The paper is organized as follows: Related work is reviewed in Sec. II. Sec. III introduces our framework for segmentation of overlapping convex objects utilizing the BE-FRS method for seedpoint extraction. The proposed method is applied to synthetic and real datasets and compared with two state-of-the-art methods in Sec. IV. Conclusions are drawn in Sec. V.

II. RELATED WORK

Several approaches have been attempted to address the segmentation of overlapping objects in different kinds of images [1]–[3], [7]–[9]. The watershed transform is one of the commonly used approaches in overlapping cell segmentation [7], [10], [11]. Exploiting a certain strategies for the initialization, such as morphological filtering [7] or the adaptive H-minima transform [10], the watershed transform may overcome the over-segmentation problem and could be used for segmentation of overlapping objects. Methods based on the watershed transform may experience difficulties with segmentation of highly overlapped objects in which a strong gradient is not present.

Graph-cut is an alternative approach for segmentation of overlapping objects [12], [13]. Al-Kofahi et al. [12] introduced a semi-automatic approach for detection and segmentation of cell nuclei where the detection process is performed by graph-cuts-based binarization and Laplacian-of-Gaussian filtering. The method is computational expensive and may fail to keep the global optimality of graph cut [14]. Daněk et al. [13] overcomed the problem of overlapping cell separation by introducing shape priors to graph-cut framework.

Another group of approaches is based on concave point extraction. Zhang et al. [2] and Bai et al. [15] addressed the problem of overlapping objects segmentation using concave points extraction through the polygonal approximation. The concave points in the objects contour divide the contour of overlapping objects into different segments based on the location of concavities and ellipse fitting is then applied to separate the overlapping objects. As these approaches strongly rely on ellipse fitting to segment object contours, they may have problems with either objects boundaries containing large scale fluctuations or objects whose shape deviate from ellipse.

Several approaches have resolved the segmentation of overlapping objects within the variational framework through the use of active contours. The method in [16] incorporates a physical shape model in terms of modal analysis that combines object contours and a prior knowledge about the expected shape into an Active Shape Model (ASM) to detect the invisible boundaries of a single nucleus. The original form of ASM is restricted to single object segmentation and cannot deal with more complex scenarios of multiple occluded objects. ASM was extended in [17] and [18] to address the segmentation of multiple overlapping objects simultaneously. The efficiency of the active contour based methods for segmentation of overlapping objects depends closely on the accurate initialization of the active active contour model.

Morphological operations have also been applied to overlapping object segmentation. Park et al. [1] proposed an automated morphology analysis coupled with a statistical model for contour inference to segment partially overlapping nanoparticles. Ultimate erosion modified for convex shape objects is used for particles separation, and the problem of object inference and shape classification are solved simultaneously using a Gaussian mixture model on B-splines. The method may be prone to under-segmentation with highly overlapped objects.

III. OVERLAPPING OBJECT SEGMENTATION

The proposed method consists of three consecutive main steps: seedpoint extraction, contour evidence extraction, and contour estimation. Fig. 2 summarizes the method.

Given a grayscale image as input, the segmentation process starts with pre-processing to build the image silhouette and the corresponding edge map. The binarization of the image is obtained by background suppression based on the Otsu's method [19]. The edge map is constructed using the Canny edge detector [20].

The seedpoints are detected by Bounded Erosion (BE) followed by the Fast Radial Symmetry (FRS) transform [6]. The purpose of BE before FRS is only to improve the quality of seedpoint extraction and the rest of process is applied to original objects. Contour evidence is extracted by edge-to-seedpoint association using the obtained seedpoints and their relation to the image edges. The contour estimation is implemented through a non-linear ellipse fitting problem in which partially observed objects are modelled in the form of ellipse-shape objects.

A. Seedpoint Extraction

The seedpoint extraction plays a key role in overlapping object segmentation and influences significantly the accuracy of the final segmentation result. Seedpoints are considered as a certain priori information, which affects the performance of the subsequent contour evidence extraction and contour estimation. The primary goal in seedpoint extraction is to recognize the presence and number of the individual objects in the image as identified by the seedpoints.

Several approaches may be employed for seedpoint extraction. Distance Transform (DT) [21] is an operator commonly applied to image segmentation. Provided that the cores of the objects are separable, i.e. there is only a single local maximum in each object region, DT combined with a global thresholding scheme can be used to separate and to count the overlapping objects. In watershed transformation, the local maxima regions of DT are watershed markers which eventually result in the segmentation of the objects. DT assumes separability of object cores and fails when the cluster of objects is highly overlapped.

Ultimate Erosion for Convex Sets (UECS) [1] is an iterative morphological algorithm that extracts the seed regions from overlapping objects. UECS is an extension of the Ultimate Erosion (UE) method with a modified stopping criteria. The early stopping of the erosion process in UECS is the key feature to overcome the problem of over-segmentation. UECS makes strict assumptions regarding the separability of objects, that cannot separate three overlapping objects with more than one intersecting point and a pair of objects whose subtraction is disconnected. Either a triple highly overlapping objects or a pair of crossing objects are not separable by UECS.

The Slide Band Filter (SBF), which belongs to the family of local convergence filters has previously been applied to detect cell nuclei and to estimate shape [22]. SBF integrates the ideas of the IRIS Filter (IF) [23] and Adaptive Ring Filter (ARF) [24] by defining a support region that has a fixed width convergence band and varying radius in each direction. SBF estimates the overall convergence by combining all the individual convergence degrees of sample points in such way that the convergence of the pixel interest point is maximized along each radial direction.

The proposed BE-FRS method for seedpoint extraction considers two generic properties of the objects under segmentation: convexity and symmetry. Inspired by the idea of morphological erosion for separating of convex-shape objects [1], BE consisting of a predefined number of erosions is first applied to extract the separable seed regions, and then FRS with duplicate seed point removal evaluates the extracted seed regions for rotational symmetry to produce the final seedpoints.

In mathematical morphology, given a binary silhouette I as a union of overlapping convex objects C_i, $I = \cup_{i=1}^{n} C_i$, BE is performed by applying a recursive number of erosion operations to increase the separability of every subset C_i. That is, at the tth iteration of the erosion process, each connected component A_i of the image silhouette $I^{(t-1)}$ is subject to Minkowski subtraction [5] with respect to a closed disc structuring element $B(0, 1)$ of the radius 1 defined as

$$R_i = A_i^{(t)} \ominus B(0, 1), \tag{1}$$

where $\ominus$ stands for Minkowski subtraction defined by

$$A_i^{(t)} \ominus B(0, 1) = \cap_{\beta \in B}(A_i^{(t)} + \beta) \tag{2}$$

and R_i is the result of the erosion process of each connected component by which the image silhouette $I^{(t)}$ is evolved

$$I^{(t+1)} = \cup_i R_i. \tag{3}$$

Fast radial symmetry (FRS) transform [6] is a feature extraction technique that transforms the original image to a new representation that highlights the local radial symmetry of the image gradient. In [25] FRS is applied for yeast colonies counting.

The main idea behind FRS transform is that every edge pixel point of the image space gives a vote for the plausible radial symmetry at some specific distance from that point. Technically, given the distance value m of the range $[R_{min} R_{max}]$, for every pixel (x, y) of the gradient image g, FRS determines the positively-affected p_{+ve} and negatively-affected p_{-ve} pixels, and sequentially constructs the orientation projection image O_m and the magnitude projection image M_m as follows:

$$p_{+ve}(x, y) = (x, y) + round\left(\frac{g(x, y)}{\|g(x, y)\|} \times m\right),$$
$$p_{-ve}(x, y) = (x, y) - round\left(\frac{g(x, y)}{\|g(x, y)\|} \times m\right) \tag{4}$$

$$O_m(p_{+ve}(x, y)) = O_m(p_{+ve}(x, y)) + 1,$$
$$O_m(p_{-ve}(x, y)) = O_m(p_{-ve}(x, y)) - 1 \tag{5}$$

$$M_m(p_{+ve}(x, y)) = M_m(p_{+ve}(x, y)) + \|g(x, y)\|,$$
$$M_m(p_{-ve}(x, y)) = M_m(p_{-ve}(x, y)) - \|g(x, y)\| \tag{6}$$

Upon constructing the orientation and magnitude images, the radial symmetry contribution S_m for the radius $m \in [R_{min}, R_{max}]$ is calculated by the convolution of F_m with a 2D Gaussian A_m:

$$S_m = F_m * A_m, \tag{7}$$
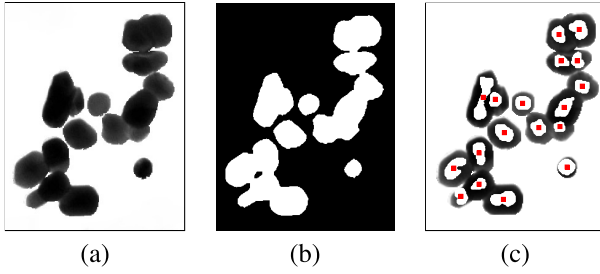
(a)   (b)   (c)

Fig. 3. Seedpoint extraction by BE-FRS: (a) Original grayscale image; (b) Binary image after morphological erosion; (C) Seedpoints identified by FRS.

where F_m is formulated as

$$F_m(x, y) = \frac{M_m(x, y)}{k_m} \left(\frac{|\tilde{O}_m(x, y)|}{k_m} \right)^{\alpha},\qquad(8)$$

α and k_m are respectively the radial strictness and the scaling factor that normalizes M_m and O_m across different radii. $\tilde{O}_m$ is defined as

$$\tilde{O}_m(x, y) = \begin{cases} O_m(x, y), & \text{if } O_m(x, y) < k_m. \\ k_m, & \text{otherwise.} \end{cases}\qquad(9)$$

The full FRS transform S by which the interest symmetric regions are defined is given by the average of the symmetry contributions over all the radii $m \in [R_{min}, R_{max}]$ considered:

$$S = \frac{1}{|N|} \sum_{m \in [R_{min}, R_{max}]} S_m.\qquad(10)$$

Eventually, the seedpoints are estimated as the average locations, centroids, of the detected symmetric regions, in S.

Fig. 3 illustrates BE-FRS applied for seedpoint extraction.

B. Contour Evidence Extraction

The contour evidence extraction is carried out by an edge-to-seed point association method [1] incorporating the visual parts of the overlapping objects and the detected seedpoints. Specifically, the edge-to-seedpoint association method combines the distance and the divergence index (cosine distance) to assign edge pixel points to the seedpoints. Given the set of object seedpoints $S = \{s_1, s_2, \ldots, s_n\}$, every edge pixel point e_k in $E = \{e_1, e_2, \ldots, e_m\}$ is linked to the detected object seedpoints based on the relevance metric $rel(e_k, s_j)$ defined as

$$rel(e_k, s_j) = \frac{1 - \lambda}{1 + dist(e_k, s_j)} + \lambda \frac{div(e_k, s_j) + 1}{2}\qquad(11)$$

where $dist(.,.)$ and $div(.,.)$ are respectively Euclidean distance and divergence functions, each normalized to (0,1] and then summed up by the weight λ. By this means, the edge point e_k is assigned to seedpoint s_j with the highest relevance value.

The distance function $dist(.,.)$ is defined as the distance from the edge point e_k to the nearest seedpoint s_j. It is assumed that all the pixel points on the line connecting the
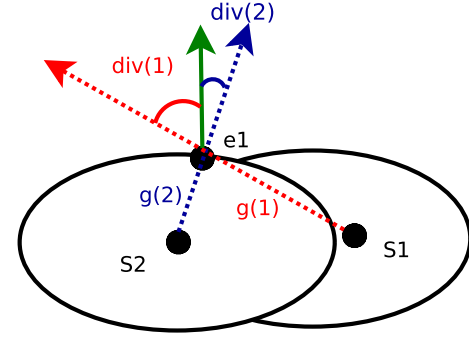

Fig. 4. Illustrative example of edge-to-seedpoint association.
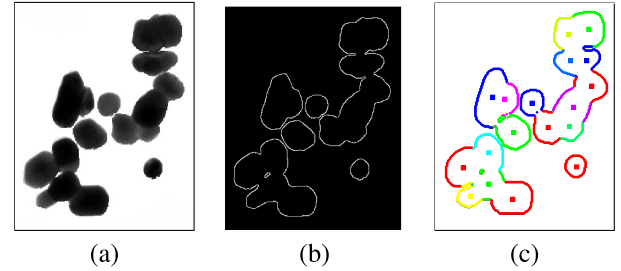

(a)   (b)   (c)

Fig. 5. Contour evidence extraction performed by edge-to-seedpoint association: (a) Original grayscale image; (b) Gradient image; (c) Edge-to-seedpoint association (the colors are used only for illustrative purpose to visualize the edge-to-seedpoint association).

edge point to the seedpoint $l(e_k, s_j)$ reside in the image foreground M:

$$g(x) = \begin{cases} |e_k - s_j|, & \text{if } l(e_k s_j) \subset M. \\ \infty, & \text{otherwise.} \end{cases}\qquad(12)$$

The divergence function $div(e_k, s_j)$ measures the difference between the direction of the line connecting the edge point e_k to seedpoint s_j and the gradient direction at point e_k, estimated by the cosine of the angle between them:

$$div(e_k, s_j) = \frac{g(e_k)l(e_k, s_j)}{\|g(e_k)\| \|l(e_k, s_j)\|}.\qquad(13)$$

In this work, to reduce the number of potential false classified edge points and the amount of computation, the search space is dynamically defined by a circular zone around each individual edge point such that fewer seedpoints are processed.

Fig. 4 demonstrates the edge-to-seedpoint association. While the green solid arrow represents the gradient direction at edge point e_1, the red and blue dashed arrows represent the direction of the lines connecting e_1 to s_1 and s_2 respectively. Fig. 5 shows the edge-to-seedpoint association applied to extract contour evidences.

C. Contour Estimation

Once the contour evidence has been obtained, contour estimation is carried out to infer the missing parts of the overlapping objects. In this work, the contour estimation is addressed through a classical ellipse fitting problem in which

the partially observed objects are modeled in the form of ellipse-shape objects.

Given set of data points (x, y), an objective cost function characterizing the goodness of the ellipse is optimized based on algebraic deviation. In algebraic ellipse fitting [26], an ellipse as a special case of a generic conic is formulated by the zero set of the second order polynomial equation. For a given point (x, y) an ellipse with a parameter vector $\boldsymbol{a}$ is defined as the equation

$$a_0 x^2 + a_1 xy + a_2 y^2 + a_3 y + a_4 y + a_5 = 0, \quad (14)$$

where

$$\boldsymbol{a} = \begin{bmatrix} a_0 & a_1 & a_2 & a_3 & a_4 & a_5 \end{bmatrix}$$

Eq. 14 defines an ellipse, provided that the quadratic condition $\Delta < 0$

$$\Delta = a_1^2 - 4a_0 a_2 < 0 \quad (15)$$

is satisfied. The goodness of the ellipse fitting is modeled as the sum of squared algebraic distances of every point involved. Given the ellipse parameter vector model $\boldsymbol{a}$, the algebraic distance $\boldsymbol{d}(\boldsymbol{a}, (x, y))$ is the deviation of point (x, y) when applied to the implicit polynomial conic equation as

$$\boldsymbol{d}(\boldsymbol{a}, (x, y)) = a_0 x^2 + a_1 xy + a_2 y^2 + a_3 y + a_4 y + a_5 \quad (16)$$

For the given set of points $\{(x_i, y_i) \mid i = 1, 2, \ldots, n\}$ the objective cost function is

$$\hat{\boldsymbol{a}} = \arg \min_{\boldsymbol{a}} \sum_{i=1}^{n} \boldsymbol{d}_i(\boldsymbol{a}, (x_i, y_i))^2. \quad (17)$$

Equivalently, collecting the data points into a design matrix $D \in \mathcal{R}^{n \times 6}$ as

$$\boldsymbol{D} = \begin{bmatrix} x_1^2 & x_1 y_1 & y_1^2 & x_1 & y_1 & 1 \\ x_2^2 & x_2 y_2 & y_2^2 & x_2 & y_2 & 1 \\ \vdots & \vdots & \vdots & \vdots & \vdots & \vdots \\ x_n^2 & x_n y_n & y_n^2 & x_n & y_n & 1 \end{bmatrix}, \quad (18)$$

the objective function can be re-formulated through the matrix representation

$$\begin{aligned} d(\boldsymbol{a}) &= \|\boldsymbol{D}\boldsymbol{a}\| \\ &= \boldsymbol{a}^T \boldsymbol{D}^T \boldsymbol{D}\boldsymbol{a} \\ &= \boldsymbol{a}^T \boldsymbol{S}\boldsymbol{a}, \quad (19) \end{aligned}$$

where $\boldsymbol{S} = \boldsymbol{D}^T \boldsymbol{D}$ is a scatter matrix.

In essence, the matrix form representation of the ellipse fitting problem in Eq. 19 along the quadratic condition in matrix form

$$\boldsymbol{a}^T \boldsymbol{C}\boldsymbol{a} < 0 \quad (20)$$

with the constrain matrix

$$\boldsymbol{C} = \begin{bmatrix} 0 & 0 & -2 & 0 & 0 & 0 \\ 0 & 1 & 0 & 0 & 0 & 0 \\ -2 & 0 & 0 & 0 & 0 & 0 \\ 0 & 0 & 0 & 0 & 0 & 0 \\ 0 & 0 & 0 & 0 & 0 & 0 \\ 0 & 0 & 0 & 0 & 0 & 0 \end{bmatrix}, \quad (21)$$
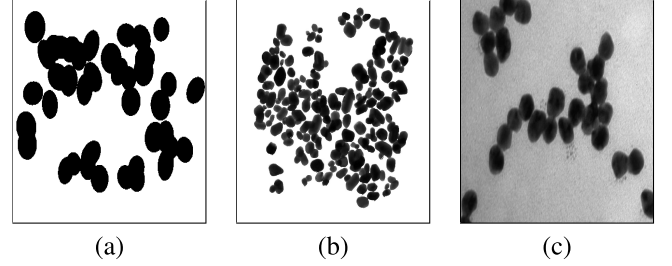

Fig. 6. Example images from the datasets studied: (a) Synthetic dataset with the maximum overlap of 40%; (b) Crystal particles dataset; (c) Nanoparticle dataset.

is the underlining formulation to resolve the minimization problem by adopting generic conics polynomial equations. However, to guarantee that the solution is an ellipse, specific auxiliary conditions need to be considered. Within the family of direct least squares ellipse fitting, the quadratic condition of Eq. 15 is replaced by

$$\Delta = a_1^2 - 4a_0 a_2 = -1, \quad (22)$$

or equivalently

$$\boldsymbol{a}^T \boldsymbol{C}\boldsymbol{a} = -1. \quad (23)$$

Given the Lagrange multiplier λ and differentiation

$$\boldsymbol{D}^T \boldsymbol{D}\boldsymbol{a} + 2\lambda \boldsymbol{C}\boldsymbol{a} = 0, \quad (24)$$

the minimization problem in its original form [27] is to resolve the following system of equations

$$\begin{aligned} \boldsymbol{S}\boldsymbol{a} &= \lambda \boldsymbol{C}\boldsymbol{a} \\ \boldsymbol{a}^T \boldsymbol{C}\boldsymbol{a} &= -1 \quad (25) \end{aligned}$$

which can be obtained explicitly through a rank-deficient generalized eigen-system for the parameter vector $\boldsymbol{a}$.

IV. EXPERIMENTS

This section, presents the data, the performance measures, parameter selection and results for seedpoint extraction and segmentation.

A. Data

The experiments were carried out using one syntheti-cally generated dataset and two datasets from real-world applications.

The synthetic dataset (Fig. 6(a)) consists of images with overlapping ellipse-shape objects that are uniformly randomly scaled, rotated, and translated. Three subsets of images are generated to represent different degrees of overlap between objects. The dataset consists of 150 sample images divided into three classes of overlap degree. The maximum rates of overlapping area allowed between two objects are 40%, 50%, and 60%, respectively, for the first, second, and third subset. Each subset of images in the dataset contains 50 images of 40 objects. The minimum and maximum width and length of the ellipses are 30, and 45 pixels. The image size is 300×400 pixels.

The first real dataset (crystal particles dataset) contains crystal particles images captured by transmission electron

microscopy (Fig. 6(b)). In total, the dataset contains 11 images of 4008 × 2672 pixels. Around 200 particles are marked manually in each image by an expert. The annotations consist of manually drawn contours of the objects. This information is, additionally, used to determine the centroids and annotated edge points. Since not all the objects are marked, a pre-processing step is applied to eliminate the unmarked objects from the images. It should be noted that the images consist of dark objects on a white background and, therefore, pixels outside the marked objects could be colored white without making the images considerably easier to analyze.

The second real dataset (nanoparticles dataset), originally presented in [1], consists of 9 micrography images of nanoparticles divided into two classes, medium and high degree of overlap (Fig. 6(c)). The dataset is used to replicate the experiments of the original publication with the method presented in this paper included. The ground truth for the object contours is not available and, therefore, the method evaluation is performed based on the manually counted total number of correctly detected particles in each image.

B. Performance Measures

To evaluate the method performance and to compare the methods, two specific performance measures, True Positive Rate (TPR) and Positive Predictive Value (PPV), were used:

$$TPR = \frac{TP}{TP + FN} \quad (26)$$

$$PPV = \frac{TP}{TP + FP} \quad (27)$$

where True Positive (TP) is the number of correctly detected seedpoints or segmented objects, False Positive (FP) is the number of incorrectly detected seedpoints or segmentation results, and False Negative (FN) is the number of missed seedpoints or objects.

To determine whether a seedpoint was correctly detected (TP), the distance to the ground truth object center was computed and the decision was made using a predefined threshold value (distance threshold, ρ_1). The threshold value was set to 8 pixels. The average distance (AD) from detected seedpoints to the ground truth object center point was used as the third performance measure for the seedpoint extraction.

To decide whether the segmentation result was correct or incorrect, Jaccard Similarity coefficient (JSC) [28] was used. Given a binary map of the segmented object O_s and the ground truth particle O_g, JSC is computed as

$$JSC = \frac{O_s \cap O_g}{O_s \cup O_g}. \quad (28)$$

The threshold values for the ratio of overlap (JSC threshold, ρ_2) were set to 0.5 and 0.7 in the real and synthetic datasets respectively. Since the synthetic dataset contains perfect ellipses and the contour estimation applied by ellipse fitting the threshold value was set to higher value than in real dataset where the object are not perfect ellipses. The average JSC (AJSC) value was also used as a third measure to evaluate the segmentation performance.
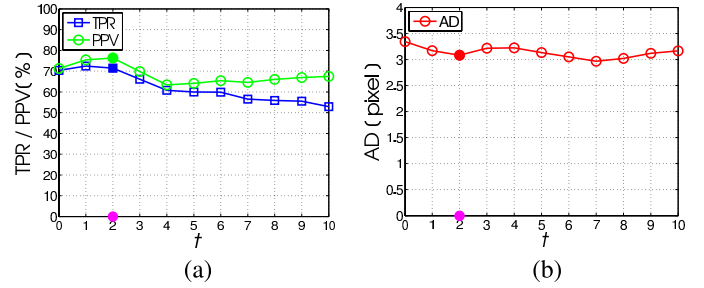

Fig. 7. Performance of seedpoint extraction for various iteration of the erosion operations in the crystal particles dataset: (a) TPR/PPV rate; (b) AD.

C. Parameter Selection

The proposed method requires the following major parameters:

Type of structuring element determines how the erosion process proceeds and affects the extent of erosions. In this work, the erosion process is performed using the disc-shaped structuring element of size one. The disc-shape structuring element is a convenient choice for smoothing concave boundaries and roundish shape objects.

Number of erosion operations (t) determines the extent of erosion, applied as a predefined number of iterations, to eliminate the touching points and increase the convexity of objects. Defining the number of erosion iterations is fairly an empirical task and is closely connected to the object size and the degree of overlap. In particular, with a very large number of erosion, it is possible that some objects with a high degree of overlap are totally faded away from the image. In this particular work, due to the large variation in size of objects and the high degree of overlap, the number of erosion operations is set to 2. Fig. 7 shows the performance of seedpoint extraction with various settings of number of erosion operations. It should be noted that since the objects size changes per each erosion operation, the radial range is adjusted.

Radial range $[R_{min}, R_{max}]$ determines the range of radii at which the FRS full transform S is computed. The radial range should be defined such that it covers the range of all objects sizes available in the image. Considering the smallest and largest object axes, the radial ranges were set to $R_{min} = 16$ and $R_{max} = 18$ for the synthetic dataset and $R_{min} = 10$ and $R_{max} = 17$ for the crystal particles dataset.

Radial-Strictness (α) defines to what extent the radial symmetry-ness of features must be weighted in the computation of the FRS full transform S. A lower value of α emphasizes on non-radially symmetric features where as a higher value of α ensures that non-radially symmetric features are eliminated. This parameter is useful when the objects are not perfectly radial symmetric.

Fig. 8 presents the effect of different values of α on the performance of the FRS algorithm applied on the crystal particles dataset. In this work, the radial strictness parameter α was set to 1 to obtain the highest performance of FRS. With varying values of α, the other parameters are kept fixed as described above.

Divergence weight factor (λ) is a scalar parameter that defines the relative importance of the divergence index with
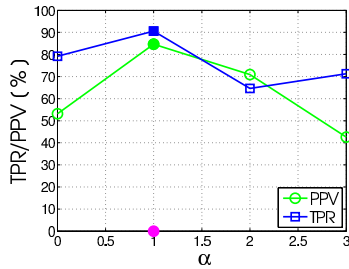
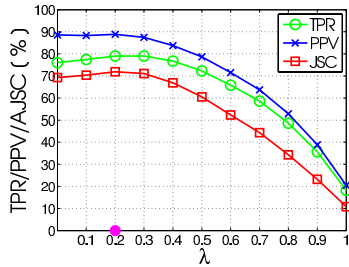Fig. 8. Performance of seedpoint extraction with different values of α in the crystal particles dataset.

Fig. 9. Performance of the proposed segmentation method with different values of λ in the crystal particles dataset.

respect to the Euclidean distance as formulated in Eq. 11. The parameter λ takes a value from the range [0, 1]. A high value ($\lambda > 0.5$) results a relevance function that outweighs divergence index to the Euclidean distance, while a low value ($\lambda < 0.5$) results a relevance function that outweighs the Euclidean distance. Determining the value of λ is closely connected to the quality of the estimated seedpoint. In general, provided accurate estimates of object seedpoints, the performance of the relevance function, assigning edge to seedpoints, is ruled by the Eculidean distance, and the value of parameter λ is not critical. However, if the estimated seedpoints do not optimally resemble the object centroids, the Euclidean distance can be ambiguous, and accordingly a large value of λ is a preferable choice.

Fig. 9 presents the effect of the various values of λ on the performance of the proposed segmentation method for the crystal particles dataset. The performance decreases at the high range [0.51]. Since the estimated seedpoints by the BE-FRS method are quite close to the center of the object the value of λ was set to 0.2.

D. Results

1) Seedpoint Extraction: The proposed method for seedpoint extraction was applied to detect the location of objects in both the synthetic and real datasets. As previously mentioned, the ground truth was not available for the nanoparticles dataset and it is excluded from seedpoint extraction comparisons.

The results for the seedpoint extraction applied to the synthetic and crystal particles datasets are presented in Tables I and II respectively. The results obtained from the synthetic dataset (see Table I) show that BE-FRS, FRS, and SBF generally achieve better performance scores than DT and UECS. While, in terms of TPR and PPV scores BE-FRS,

TABLE I

COMPARISON OF THE PERFORMANCE OF SEEDPOINT EXTRACTION METHODS ON THE SYNTHETIC DATASET

Methods	Overlapping rate[%]	TPR [%]	PPV [%]	AD [pixel]
BE-FRS	40	95	**100**	2.03
FRS	40	96	99	2.14
SBF	40	**97**	97	2.85
DT	40	70	85	**1.50**
UECS	40	50	71	2.50
BE-FRS	50	93	**100**	2.10
FRS	50	**94**	99	2.20
SBF	50	**94**	97	3.05
DT	50	65	85	**1.57**
UECS	50	83	73	2.76
BE-FRS	60	92	**100**	2.23
FRS	60	**94**	99	2.32
SBF	60	94	96	3.08
DT	60	70	82	**1.81**
UECS	60	47	72	2.98

TABLE II

COMPARISON OF THE PERFORMANCE OF THE SEEDPOINT EXTRACTION METHODS ON THE CRYSTAL PARTICLES DATASET

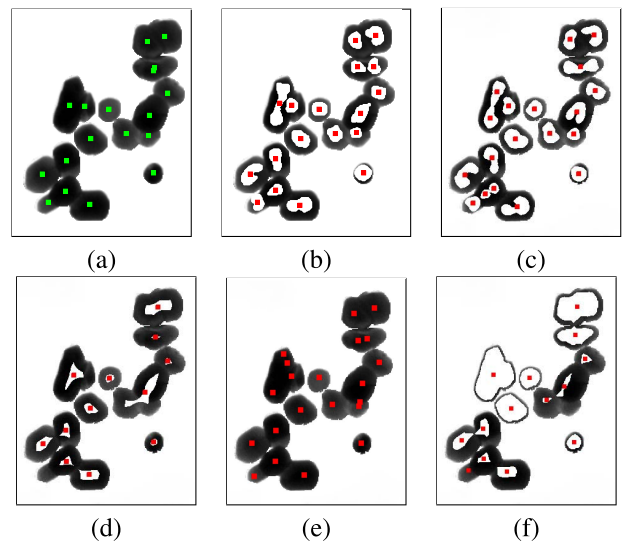| Methods	TPR [%]	PPV [%]	AD [pixel]
BE-FRS	**71**	**77**	3.08
FRS	70	71	3.33
SBF	50	46	4.39
UECS	41	68	3.56
DT	33	76	**2.61**

Fig. 10. Comparison of the performance of the seedpoint extraction methods on the crystal particles dataset: (a) Ground truth; (b) BE-FRS; (c) FRS; (d) DT; (e) SBF; (f) UECS.

FRS and, SBF methods are comparable, in terms of PPV, BE-FRS outperforms the other methods. The results in Table II show the advantage of BE-FRS over the other methods when
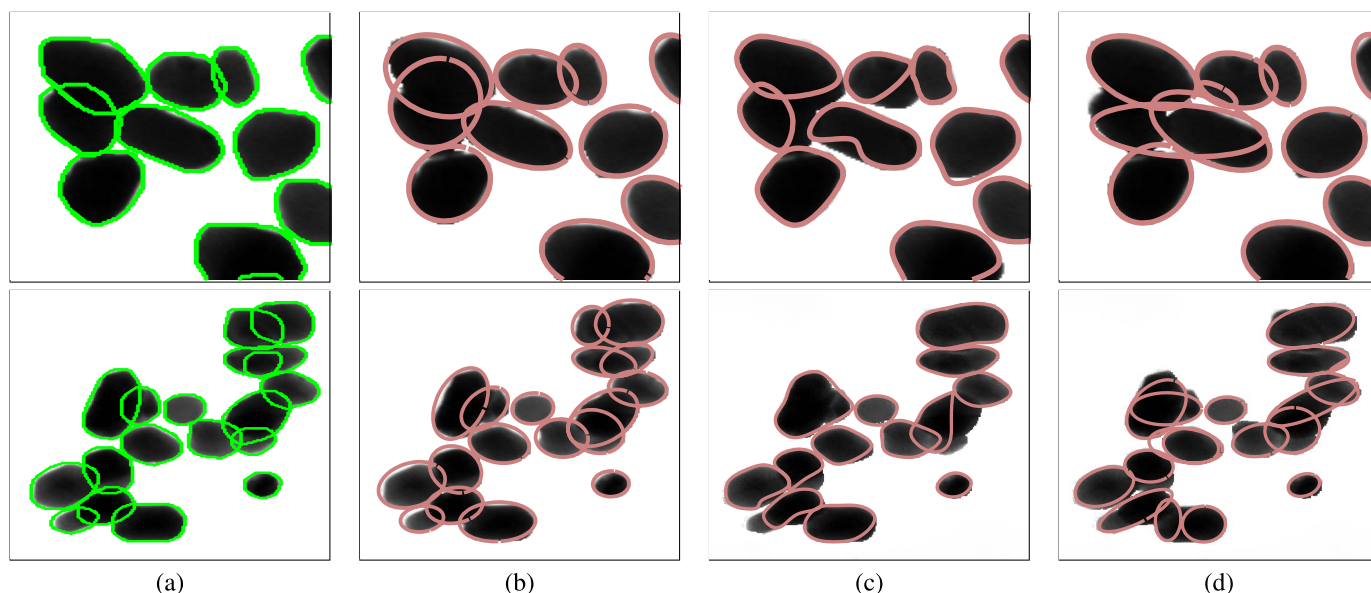
Fig. 11.   Example segmentation results on the crystal particles dataset: (a) Ground truth; (b) Proposed method; (c) NPA; (d) CECS.

TABLE III

COMPARISON OF THE PERFORMANCE OF THE PROPOSED
METHOD ON THE SYNTHETIC DATASET

Methods	overlapping rate[%]	TPR [%]	PPV [%]	AJSC [%]
Proposed	40	**93**	**95**	**89**
NPA	40	68	80	60
CECS	40	89	91	83
Proposed	50	**88**	**92**	**83**
NPA	50	61	76	53
CECS	50	82	87	73
Proposed	60	**87**	**91**	**80**
NPA	60	53	71	44
CECS	60	75	83	65

TABLE IV

COMPARISON OF THE PERFORMANCE OF THE PROPOSED
METHOD ON THE CRYSTAL PARTICLES DATASET

Methods	TPR [%]	PPV [%]	AJSC [%]
Proposed	**79**	89	**72**
NPA	62	**90**	58
CECS	66	73	53

Fig. 12.   Example segmentation results on the nanoparticles dataset:
(a) Proposed method; (b) NPA.

applied to the crystal particles dataset. While the TPR and PPV values indicate its higher accuracy, the lower AD reveals its performance in terms of seedpoint quality. Note that BE-FRS performs better than SBF in the case of the real dataset since it is more robust when the object shapes are less convex.

Fig. 10 demonstrates the result of seedpoint extraction applied to a slice of crystal particles dataset. Of the methods studied, it can be seen that BE-FRS outperforms the other methods and that while DT and UECS exhibit under-segmentation, SBF and FRS suffers from over-segmentation.

2) Segmentation: The performance of the proposed segmentation method was compared to two existing methods, Nanoparticles Segmentation (NPA) [1] and Concave-point Extraction and Contour Segmentation (CECS) [2]. The NPA and CECS methods are particularly chosen as previously applied for segmentation of overlapping convex and elliptical shape objects, respectively. The implementation made by the corresponding authors was used for NPA [1]. CECS was implemented by ourselves based on [2]. Examples of typical
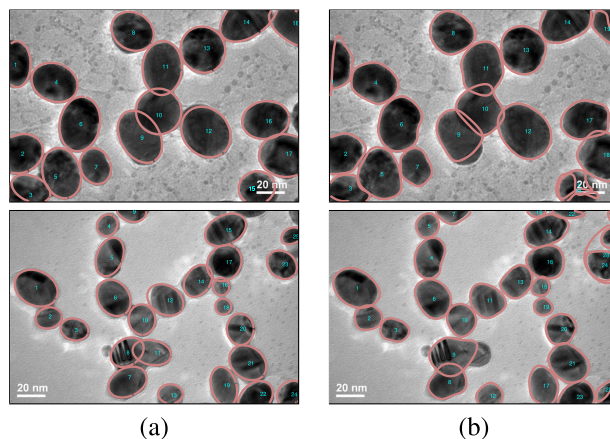
segmentation results are presented in Fig. 11. NPA suffers from undersegmentation while CECS tends to oversegment the objects. The proposed method neither under- or oversegments the objects.

The corresponding performance statistics of the competing methods applied to the synthetic and the crystal particles datasets are shown in Tables III and IV respectively. In the case of the synthetic dataset, the proposed method is the best one in all terms. This is clearly because of the fitted ellipse

TABLE V

COMPARISON OF THE METHODS ON THE NANOPARTICLES DATASET. THE NUMBERS DENOTES THE NUMBER OF CORRECTLY DETECTED PARTICLES

Sample	Degree of overlap	Total # of particles	Proposed method	NPA	N-Cut	MPAC	SBF	IVM	MSD	WHM	WHD
Sample1	medium	28	**28**	26	6	2	28	25	20	20	20
Sample2	medium	52	46	**48**	29	22	43	45	48	45	39
Sample3	medium	459	425	**437**	298	147	262	227	429	424	421
Sample4	medium	19	**18**	17	10	8	6	16	16	15	6
Sample5	medium	108	**104**	103	56	44	99	85	92	82	70
Sample6	medium	29	**25**	25	12	13	19	21	23	18	14
Sample7	high	63	52	**54**	31	12	42	42	40	38	34
Sample8	high	44	**37**	34	23	11	28	27	28	28	28
Sample9	high	45	**33**	33	20	6	25	24	22	19	20
AVG [%]			**88**	87	48	29	68	71	75	70	60
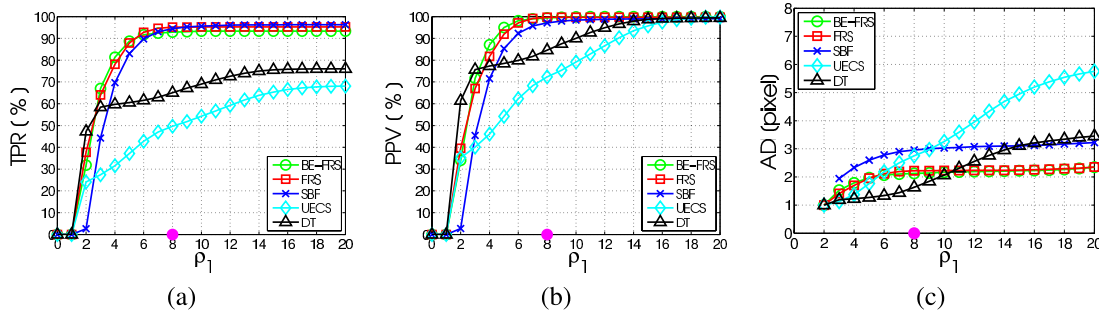
Fig. 13. Performance of seedpoint extraction with different values of the distance threshold (ρ_1) in the synthetic dataset: (a) TPR; (b) PPV; (c) AD.

model, which is in line with the elliptical shape of objects. In the case of the crystal particles dataset (Table IV), the proposed method outperforms the other two with respect to the TPR and AJSC, but in terms of PPV, NPA performs slightly better than the proposed method. The high AJSC value of the proposed method indicates its superiority with respect to the resolved overlap ratio.

Table V presents results for the nanoparticles dataset from [1] updated with the proposed method. The other methods are NPA, watershed segmentation with h-dome transform (WHD) [29], marker-controlled watershed with h-maxima transform (WHM) [30], normalized-cut (N-Cut) [31], multiphase active contour (MPAC) [32], sliding band filter (SBF) [22], morphological multi scale method MSD [33], and iterative voting method IVM [9]. Due to the non-availability of ground truth data, the performance of the methods is quantified using the total number of correctly identified objects, similar to original publication. For the images of the medium and high degree of overlap the proposed method achieves the highest segmentation rate in six images and the second-highest rate in the rest. Overall, the proposed method outperforms the competing methods in terms of average percentage of correctly detected objects. An example of segmentation on the nanoparticles dataset is presented in Fig. 12.

E. Analysis of Evaluation Parameters

The results reported above were obtained with a fixed set of evaluation parameters chosen as described in Sec. IV-B. To study the reliability of the results, the effect of the

evaluation parameters, the distance threshold (ρ_1) and JSC threshold (ρ_2), were analyzed using the synthetic and crystal particles dataset.

The effect of ρ_1 on the TPR, PPV and AD scores obtained with different seedpoint extraction methods are presented in Figs. 13 and 14. As it can be seen, the value of ρ_1 has only minor effect on the ranking order of the methods and the proposed BE-FRS method is one of the best methods regardless of the selected threshold value. In general, at low values of ρ_1, in terms of TPR, BE-FRS is the best method, while in terms of PPV and AD, DT is slightly better than BE-FRS. High PPV and AD scores of DT, reflecting the higher precision rate of detected seedpoints, are consistent with the specific formulation in DT that does not make assumption about the shape of objects.

Figs. 15 and 16 show the effect of the threshold ρ_2 on the TPR, PPV and AJSC scores with the proposed and competing segmentation methods. As expected, the segmentation performance of all methods degrades when the JSC threshold is increased. However, again, the value of ρ_2 has only minor effect on the ranking order of the methods and the proposed segmentation method outperforms the other methods with all JSC threshold values below 0.9. With the threshold value of 0.9 NPA is slightly better due to the fact that the objects are not perfect ellipses and the ellipse fitting cannot estimate the contours with such accuracy.

F. Computation Time

The proposed method was implemented in MATLAB, using a PC with a 3.20 GHz CPU and 8 GB of RAM. The processing
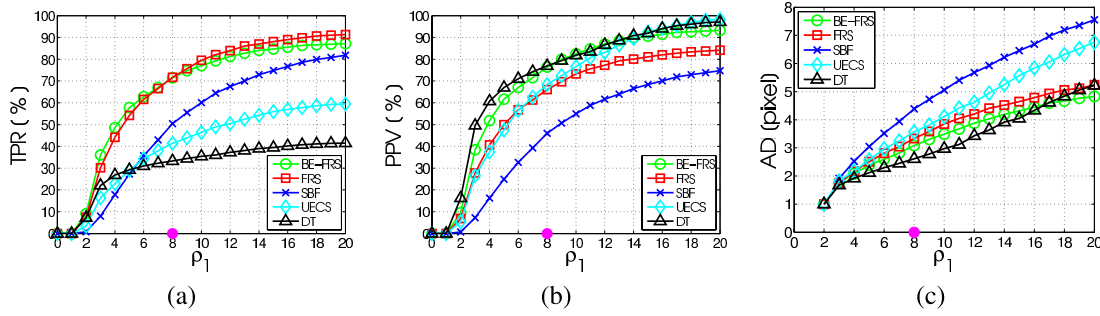
Fig. 14.   Performance of seedpoint extraction with different values of the distance threshold (ρ_1) in the crystal particles dataset: (a) TPR; (b) PPV; (c) AD.
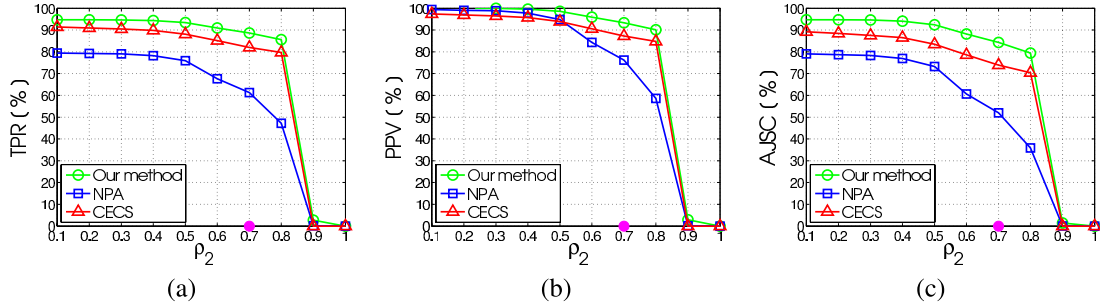

Fig. 15.   Performance of the segmentation methods with different values of the JSC threshold (ρ_2) in the synthetic dataset: (a) TPR; (b) PPV; (c) AJSC.
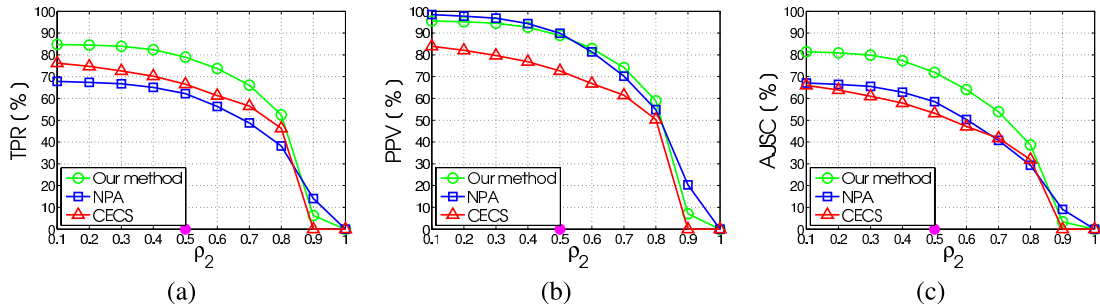

Fig. 16.   Performance of the segmentation methods with different values of the JSC threshold (ρ_2) in the crystal particles dataset: (a) TPR; (b) PPV; (c) AJSC.

time depends on the image resolution. With the selected combination of parameters the computational time was 150 seconds per crystal particle image, while NPA demanded 200 seconds and CECS 77 seconds. The computational time breakdown was as follows: seedpoint extraction 53%, edge-to marker association 45%, and ellipse fitting 2%. However, it should be noted that the method performance was not optimized and the computation time could be significantly improved.

V. Conclusions

This paper presented a method to segment multiple partially overlapping approximately elliptical shape objects in silhouette images using radial symmetry. The proposed method consists of seedpoint extraction using Bounded Erosion and Fast Radial Symmetry Transform, contour evidence extraction using edge-to-seedpoint association, and contour estimation using ellipse fitting. The experiments were carried out using one synthetically generated dataset and two datasets from real-world applications. The proposed approach for seedpoint extraction and the segmentation method were shown to achieve high

detection and segmentation accuracies and they were found to outperform the competing methods in all datasets. In future work it would be worthwhile to include the generalization of the method with more complex convex objects.

References

[1] C. Park, J. Z. Huang, J. X. Ji, and Y. Ding, "Segmentation, inference and classification of partially overlapping nanoparticles," *IEEE Trans. Pattern Anal. Mach. Intell.*, vol. 35, no. 3, pp. 669–681, Mar. 2013.

[2] W.-H. Zhang, X. Jiang, and Y.-M. Liu, "A method for recognizing overlapping elliptical bubbles in bubble image," *Pattern Recognit. Lett.*, vol. 33, no. 12, pp. 1543–1548, 2012.

[3] S. Kothari, Q. Chaudry, and M. D. Wang, "Automated cell counting and cluster segmentation using concavity detection and ellipse fitting techniques," in *Proc. IEEE Int. Symp. Biomed. Imag.*, Jun./Jul. 2009, pp. 795–798.

[4] R. Fisker, J. M. Carstensen, M. F. Hansen, F. Bødker, and S. Mørup, "Estimation of nanoparticle size distributions by image analysis," *J. Nanoparticle Res.*, vol. 2, no. 3, pp. 267–277, 2000.

[5] R. M. Haralick, S. Zhuang, C. Lin, and J. Lee, "The digital morphological sampling theorem," *IEEE Trans. Acoust., Speech Signal Process.*, vol. 37, no. 12, pp. 2067–2090, Dec. 1989.

[6] G. Loy and A. Zelinsky, "Fast radial symmetry for detecting points of interest," *IEEE Trans. Pattern Anal. Mach. Intell.*, vol. 25, no. 8, pp. 959–973, Aug. 2003.

[7] J. Shu, H. Fu, G. Qiu, P. Kaye, and M. Ilyas, "Segmenting overlapping cell nuclei in digital histopathology images," in *Proc. 35th Annu. Int. Conf. Eng. Med. Biol. Soc. (EMBC)*, Jul. 2013, pp. 5445–5448.

[8] P. Quelhas, M. Marcuzzo, A. M. Mendonça, and A. Campilho, "Cell nuclei and cytoplasm joint segmentation using the sliding band filter," *IEEE Trans. Med. Imag.*, vol. 29, no. 8, pp. 1463–1473, Aug. 2010.

[9] B. Parvin, Q. Yang, J. Han, H. Chang, B. Rydberg, and M. H. Barcellos-Hoff, "Iterative voting for inference of structural saliency and characterization of subcellular events," *IEEE Trans. Med. Imag.*, vol. 16, no. 3, pp. 615–623, Mar. 2007.

[10] J. Cheng and J. C. Rajapakse, "Segmentation of clustered nuclei with shape markers and marking function," *IEEE Trans. Biomed. Eng.*, vol. 56, no. 3, pp. 741–748, Mar. 2009.

[11] C. Jung and C. Kim, "Segmenting clustered nuclei using H-minima transform-based marker extraction and contour parameterization," *IEEE Trans. Biomed. Eng.*, vol. 57, no. 10, pp. 2600–2604, Oct. 2010.

[12] Y. Al-Kofahi, W. Lassoued, W. Lee, and B. Roysam, "Improved automatic detection and segmentation of cell nuclei in histopathology images," *IEEE Trans. Biomed. Eng.*, vol. 57, no. 4, pp. 841–852, Apr. 2010.

[13] O. Daněk, P. Matula, C. Ortiz-de-Solórzano, A. Muñoz-Barrutia, M. Maška, and M. Kozubek, "Segmentation of touching cell nuclei using a two-stage graph cut model," in *Image Analysis* (Lecture Notes in Computer Science), vol. 5575, A.-B. Salberg, J. Y. Hardeberg, and R. Jenssen, Eds. New York, NY, USA: Springer-Verlag, 2009, pp. 410–419.

[14] X. Lou, U. Koethe, J. Wittbrodt, and F. A. Hamprecht, "Learning to segment dense cell nuclei with shape prior," in *Proc. IEEE Conf. Comput. Vis. Pattern Recognit. (CVPR)*, Jun. 2012, pp. 1012–1018.

[15] X. Bai, C. Sun, and F. Zhou, "Splitting touching cells based on concave points and ellipse fitting," *Pattern Recognit.*, vol. 42, no. 11, pp. 2434–2446, 2009.

[16] Y. N. Law, H. K. Lee, C. Liu, and A. M. Yip, "A variational model for segmentation of overlapping objects with additive intensity value," *IEEE Trans. Image Process.*, vol. 20, no. 6, pp. 1495–1503, Jun. 2011.

[17] Q. Zhang and R. Pless, "Segmenting multiple familiar objects under mutual occlusion," in *Proc. IEEE Int. Conf. Image Process. (ICIP)*, Oct. 2006, pp. 197–200.

[18] S. Ali and A. Madabhushi, "An integrated region-, boundary-, shape-based active contour for multiple object overlap resolution in histological imagery," *IEEE Trans. Med. Imag.*, vol. 31, no. 7, pp. 1448–1460, Jul. 2012.

[19] N. Otsu, "A threshold selection method from gray-level histograms," *Automatica*, vol. 11, nos. 285–296, pp. 23–27, 1975.

[20] J. Canny, "A computational approach to edge detection," *IEEE Trans. Pattern Anal. Mach. Intell.*, vol. PAMI-8, no. 6, pp. 679–698, Nov. 1986.

[21] A. Rosenfeld and J. L. Pfaltz, "Sequential operations in digital picture processing," *J. ACM*, vol. 13, no. 4, pp. 471–494, 1966.

[22] C. S. Pereira, H. Fernandes, A. M. Mendonça, and A. Campilho, "Detection of lung nodule candidates in chest radiographs," in *Pattern Recognition and Image Analysis* (Lecture Notes in Computer Science), vol. 4478. New York, NY, USA: Springer-Verlag, 2007, pp. 170–177.

[23] H. Kobatake and S. Hashimoto, "Convergence index filter for vector fields," *IEEE Trans. Image Process.*, vol. 8, no. 8, pp. 1029–1038, Aug. 1999.

[24] J. Wei, Y. Hagihara, and H. Kobatake, "Detection of cancerous tumors on chest X-ray images—Candidate detection filter and its evaluation," in *Proc. Int. Conf. Image Process. (ICIP)*, vol. 3. 1999, pp. 397–401.

[25] J. Schier and B. Kovář, "Automated counting of yeast colonies using the fast radial transform algorithm," in *Proc. Int. Conf. Bioinform. Models, Methods Algorithms*, 2011, pp. 22–27.

[26] M. Pilu, A. W. Fitzgibbon, and R. B. Fisher, "Ellipse-specific direct least-square fitting," in *Proc. Int. Conf. Image Process. (ICIP)*, vol. 3. Sep. 1996, pp. 599–602.

[27] A. Fitzgibbon, M. Pilu, and R. B. Fisher, "Direct least square fitting of ellipses," *IEEE Trans. Pattern Anal. Mach. Intell.*, vol. 21, no. 5, pp. 476–480, May 1999.

[28] S.-S. Choi, S.-H. Cha, and C. C. Tappert, "A survey of binary similarity and distance measures," *J. Syst., Inform.*, vol. 8, no. 1, pp. 43–48, 2010.

[29] N. Malpica *et al.*, "Applying watershed algorithms to the segmentation of clustered nuclei," *Cytometry*, vol. 28, no. 4, pp. 289–297, 1997.

[30] E. Bengtsson, C. Wählby, and J. Lindblad, "Robust cell image segmentation methods," *Pattern Recognit. Image Anal.*, vol. 14, no. 2, pp. 157–167, 2004.

[31] J. Shi and J. Malik, "Normalized cuts and image segmentation," *IEEE Trans. Pattern Anal. Mach. Intell.*, vol. 22, no. 8, pp. 888–905, Aug. 2000.

[32] L. A. Vese and T. F. Chan, "A multiphase level set framework for image segmentation using the Mumford and shah model," *Int. J. Comput. Vis.*, vol. 50, no. 3, pp. 271–293, 2002.

[33] O. Schmitt and M. Hasse, "Morphological multiscale decomposition of connected regions with emphasis on cell clusters," *Comput. Vis. Image Understand.*, vol. 113, no. 2, pp. 188–201, 2009.

[34] S. Zafari, "Segmentation of overlapping convex objects," M.S. thesis, School Ind. Eng. Manage., Degree Program Comput. Sci., Lappeenranta Univ. Technol., Lappeenranta, Finland, 2014.

Sahar Zafari received the M.Sc. degree in intelligent computing from the Department of Industrial Engineering and Management, Lappeenranta University of Technology, Finland, in 2014. She is currently pursuing the Ph.D. degree with the School of Engineering Science, Machine Vision and Pattern Recognition Laboratory, Lappeenranta University of Technology. Her research focus is on image processing more specifically segmentation of overlapping objects.

Tuomas Eerola received the M.Sc. and Ph.D. degrees in information processing from the Department of Information Technology, Lappeenranta University of Technology, Finland, in 2006 and 2010, respectively. He is currently a Post-Doctoral Researcher with the Machine Vision and Pattern Recognition Laboratory, Lappeenranta University of Technology. His research interests include digital image processing, pattern recognition, and image quality assessment.

Jouni Sampo received the Ph.D. degree in applied mathematics from the Department of Mathematics and Physics, Lappeenranta University of Technology, Finland, in 2010, where he is currently a University Lecturer with the Department of Mathematics and Physics. His main research interest is theory and applications of harmonic analysis, especially multiscale transforms in image processing.

Heikki Kälviäinen has been a Professor of Computer Science and Engineering with the Machine Vision and Pattern Recognition Laboratory, Lappeenranta University of Technology (LUT), Finland, since 1999. He has also been a Visiting Professor with the Brno University of Technology, Czech Technical University, and the University of Surrey. He is currently a Professor of Computing with Monash University Malaysia. His primary research interests include machine vision, pattern recognition, and digital image processing and analysis.

Heikki Haario has been a Professor of Applied Mathematics with the Lappeenranta University of Technology since 2005. He is currently a part-time Research Professor with the Finnish Meteorological Institute. His interests include inverse problems and uncertainty quantification. His research group is part of the Finnish Academy CoE in inverse problems. His current research topics include adaptive MCMC and data-assimilation algorithms.